2D Materials

PAPER

Selective growth of monolayer semiconductors for diverse synaptic junctions

To cite this article: Linfeng Sun *et al* 2019 *2D Mater.* **6** 015029

IOP Publishing 2D Mater. **6** (2019) 015029 https://doi.org/10.1088/2053-1583/aaf3d0

2D Materials

RECEIVED
30 July 2018

REVISED
6 November 2018

ACCEPTED FOR PUBLICATION
26 November 2018

PUBLISHED
17 December 2018

PAPER

Selective growth of monolayer semiconductors for diverse synaptic junctions

Linfeng Sun[1], Hua Yu[2], Dong Wang[3], Jinbao Jiang[2], Dohyun Kim[1], Hyun Kim[2], Shoujun Zheng[1], Mali Zhao[1], Qi Ge[3] and Heejun Yang[1]

[1] Department of Energy Science, Sungkyunkwan University, Suwon 16419, Republic of Korea
[2] Center for Integrated Nanostructure Physics (CINAP), Institute for Basic Science (IBS), Sungkyunkwan University, Suwon 16419, Republic of Korea
[3] Digital Manufacturing and Design Center, Singapore University of Technology and Design, Singapore 487372, Singapore

E-mail: h.yang@skku.edu

Keywords: two-dimensional materials, synaptic junctions, metal-insulator transition, defect engineering, chemical vapor deposition

Supplementary material for this article is available online

Abstract

The information computation through synapse networks in the brain plays a vital role for cognitive behaviors such as image/video recognition, self-learning, and decision-making. Achieving proper synaptic networks by conventional semiconductor and memristive devices has encountered critical issues such as the spatial density requiring a number of transistors for one synapse, reliable filament formation in memristors, or emulating diverse excitatory and inhibitory synaptic plasticity with two-terminal device geometry. Here, we report selective growth of variously doped MoS_2 with controllable conductance plasticity, which can be used for emulating diverse synaptic junctions. The conductance plasticity in the monolayer MoS_2 was found to originate from resistive-heating near the junctions with electrodes in the two-terminal device geometry and the carrier concentration-dependent metal-insulator transition in the MoS_2 channel. A spatiotemporal synaptic summation is demonstrated where the firing of a proper postsynaptic membrane potential can be designed for cognitive processes. Compared with previously reported three terminal synaptic devices with atomically thin materials, our two-terminal devices with flexible synaptic strengths have advantages for integrating three-dimensional neuronal networks. This provides a new insight on two-dimensional materials as a promising arena for integrated synaptic functionalities in artificial neural networks.

1. Introduction

In contrast to the traditional von Neumann architecture, the brain-inspired neuromorphic architecture implements memory storage and complex nonlinear operators to perform collective and distributed computation at the same time [1]. Based on the design principles of biological neural systems, it could range from serial clocked multi-neuron systems to massively-parallel asynchronous information computation and memory storage [2]. So far, remarkable brain-inspired electronic multi-neuron computing platforms at system level have been developed to realize alternative information computing for conducting pattern recognition and machine learning tasks that speed up the simulation of computational neuroscience models [3, 4]. However, the current platform, inspired by biological neural processing systems, is constrained by both precision requirements and bandwidth requirements. An alternative strategy is to emulate neural system in biology more closely by developing new materials and devices, and by designing electronic circuits that directly mimics real synapses, neurons, and other neural structures [5, 6].

It is well known that synaptic transmission stimulates the target neuron by a nerve impulse [1, 7–10], which is an omnipresent mechanism for the astonishing and complicated brain operations [10–12]. Recent advances in physiology have revealed that the stimulation of a target neuron uses different synaptic networks, composed of both excitatory and inhibitory synapses, to selectively drive emotions and behaviors [13]. Achieving diverse synaptic transmissions or spatiotemporal signal processing through different synapse networks with a high spatial density is a step forward for realizing neural networks that could determine whether a postsynaptic target neuron should be activated, leading to a decision-making process.

Conventional neuromorphic devices using complementary metal oxide semiconductors for artificial synapses require tens of transistors to mimic one synapse [3, 14]. Alternatively, memristors based on various oxides have shown synaptic plasticity in a single device [15–22], but demonstrating diverse synaptic networks with memristors still remains an issue, particularly, due to the lack of flexible synaptic plasticity. Although a junction-based synaptic device has shown versatile synaptic functions recently [23], the interface issue in the fabrication processes still needs to be more explored. Other synaptic devices based on three-terminal device would encounter the issue on three-dimensional integration of neuronal networks [24, 25]. To overcome the above issues, a resistive heating-based 2D synaptic device with two-terminal geometry has been recently reported [26]. However, direct synthesis of proper 2D materials for such synaptic devices and the exact working mechanism of the conductance plasticity with the 2D materials remain open questions.

In this work, we report carrier-density-selective growth of a monolayer MoS_2 by chemical vapor deposition (CVD) for diverse conductance plasticity (synaptic plasticity) in the MoS_2 channels; with the 2D material, we could construct synaptic spatiotemporal summation networks that are critical components in neural computation. Carefully investigating the conductance dynamics in the MoS_2, both in experiment and simulation, we could clarify the origin of the conductance plasticity in the MoS_2 which is the resistive-heating effect with residual temperature changes in the channel, especially near the MoS_2-metal electrode junctions. The diverse positive and negative temperature-resistivity correlations in the MoS_2, achieved by the carrier-density-controlled MoS_2 through the CVD process, were successfully used for the emulation of synaptic facilitation and depression and for constructing efficient synaptic networks for cognitive behaviors [1, 7].

2. Experimental methods

2.1. Selective synthesis of materials

The monolayer MoS_2 in this work was grown via the atmospheric-pressure chemical vapor deposition (APCVD) method. Commercial sulfur and sodium molybdate dihydrate were used as the source/precursor and put into a two-temperature-zone furnace. Sodium molybdate (0.1 g) was dissolved into 50 ml of deionized water, which was then stirred for longer than 30 min to dissolve the sodium molybdate completely. The sodium molybdate film was formed by spin coating at a spin rate of 3000 rpm for 30 s on a SiO_2 substrate, which was annealed at a temperature of 973 K for 10 min. After that, the SiO_2 substrate was placed downstream where it is the high temperature zone, and the sulfur was put in the low temperature zone. The CVD growth was then performed with pure nitrogen gas at a flow rate of 500 sccm. The temperatures of the two temperature zones were raised up to 483 K and 1023 K in 20 min, respectively. The temperature was maintained for 9 min for the growth, and then the furnace was cooled down naturally to room temperature. Four different groups of samples were grown with the molybdenum precursor concentrations of 0.1 g/50 ml, 0.1 g/80 ml, 0.1 g/110 ml, 0.1 g/150 ml, respectively.

2.2. Optical characterization

Raman and Photoluminescence (PL) spectra of all samples were measured by a Witec Alpha300 Confocal System installed in a glove box filled with an inert gas (argon gas); the concentrations of O_2 and H_2O in the glove box were 0.6 ppm and 0 ppm, respectively. The laser wavelength for both the Raman and PL spectra was 532 nm, and the gratings used for the Raman and PL measurements were 1800 mm^{-1} and 600 mm^{-1}, respectively. The integration times for the Raman and PL spectra were 20 s, and 10 s, respectively. The laser power was set around 0.5 mW to avoid heating of the samples during the measurements. A 100× objective (Zeiss) lens was used to focus the laser beam.

2.3. Device fabrication and electrical characterization

Before the device fabrication process, the CVD grown monolayer MoS_2 was transferred onto a fresh SiO_2/Si substrate. Then, the substrate with the monolayer MoS_2 was first spin-coated with poly(methylmethacrylate) (PMMA) 950 A4. The initial rotation speed was 500 rpm for 5 s, and then, the speed was increased to 3000 rpm for 60 s. Then, the sample was baked at 453 K on a hot plate for 2 min. Electron beam lithography (EBL) was used to conduct the electrode pattern. Finally, the samples were metallized with Cr/Au (5 nm/50 nm).

2.4. Simulation

Finite element (FE) analysis was preformed using the commercial software package ABAQUS (Simulia, Providence, RI, USA). FE analysis was performed to simulate the temperature distribution in the channel of the monolayer MoS_2-based FETs, using the ABAQUS. The model consists of two Au electrodes on the top of the monolayer MoS_2 nanobelts. In the simulation with a voltage of 5 V, the length and width of the channel were 5, and 3 μm, respectively. The Au and MoS_2 were discretized using the thermal-electrical brick element (DC3D8E). A pulse voltage is applied in the simulation and the temperature distributions over time are obtained. The material parameters used in the simulations are like below; the thermal conductivities

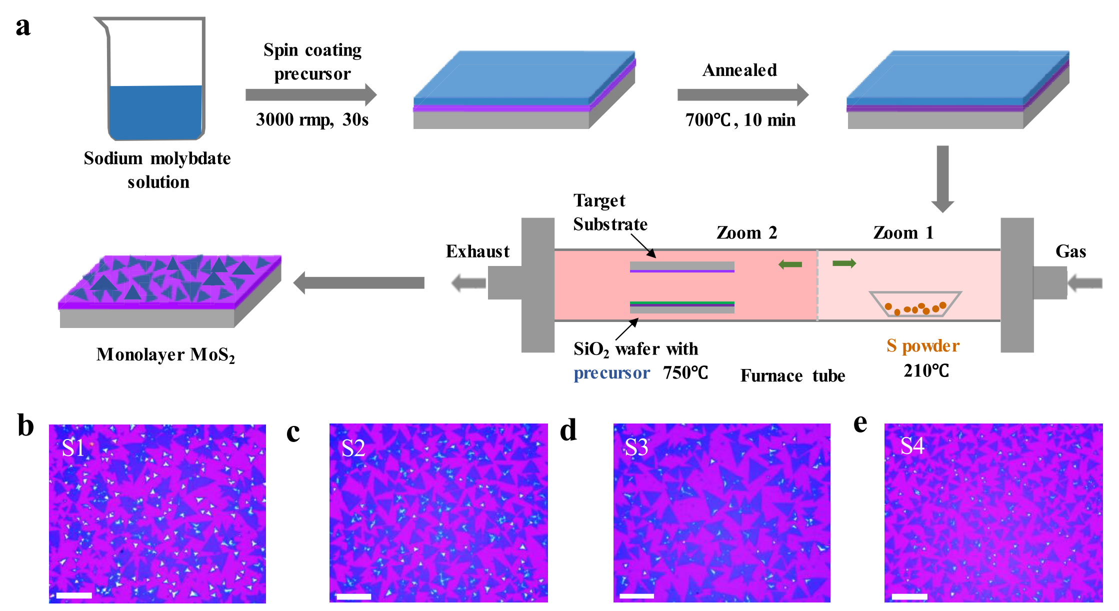

Figure 1. Schematic of selective material synthesis. (a) The experimental steps and set-up used in this work for the synthesis of four different groups of MoS_2. (b)–(e) The optical images of the four groups (G1, G2, G3, and G4) of the monolayer MoS_2 in this work.

of MoS_2 and Au are 33.6 W m^{-1} K^{-1} and 314 W m^{-1} K^{-1}, respectively; the densities of MoS_2 and Au are $5.06 * 10^3$ kg m^{-3} and $19.3 * 10^3$ kg m^{-3}, respectively; the electrical conductivities of MoS_2 and Au are 4.98 $* 10^{-3}$ S m^{-1} and $4.1 * 10^7$ S m^{-1}; the specific heat of MoS_2 and Au are 1.43 J $(kg \cdot K)^{-1}$ and 0.47 J $(kg \cdot K)^{-1}$.

2.5. Device passivation

Few-layered hexagonal boron nitride (h-BN) was used for device passivation because h-BN is a stable 2D material under ambient conditions and could prevent the oxidation of the material. In particular, an ultrathin h-BN film is impervious to oxygen diffusion even at high temperature. The experimental steps are shown in electronic supplementary information (figure S1) (stacks.iop.org/TDM/6/015029/mmedia). First, thin h-BN nanoflakes were mechanically exfoliated onto a SiO_2/Si substrate, which was then covered with a dual-layer polymer stack of poly(vinyl alcohol) (PVA) and PMMA. The bottom layer (PVA) was dissolved in DI water, and then, the remaining membrane (PMMA with exfoliated h-BN nanoflakes) was inverted and positioned above the target device assisted by optical microscopy.

2.6. Description of the neuroscientific application with our short-term plasticity in MoS_2

Neuromorphic computing has been proposed and implemented to overcome the bottleneck from the classical von Neumann architectures-based computers [1]. In neuromorphic computing, artificial synapses with short-term and long-term synaptic plasticity are the vital components to emulate the bio-synaptic function [27]. It is well known that, through a biological synapse, neural signal transfer occurs from presynaptic to postsynaptic neurons [7]. From the viewpoint of device, a corresponding artificial synapse could be created using our MoS_2 based resistors. In neuromorphic science, the spike signal transferred through the synapse, the synapse exhibits a higher (lower) amplitude of transmitted excitatory (inhibitory) postsynaptic current, called synaptic facilitation (depression) with a higher synaptic strength [8, 28]. In our device, due to the joule heating effect, the hysteresis appeared in the *I*–*V* curves can mimic a short-term memory effect, and the increasing (decreasing) conductance of device materials with more cycling number is considered as the synaptic strength facilitation (depression). After the remove of applied voltage, the conductance of material could recover its original value due to the nature cooling, which exactly mimics the short-term plasticity in neuromorphic science.

3. Results and discussion

We synthesized a monolayer 2H–MoS_2 by the air-pressure chemical vapor deposition (APCVD) method on a clean silicon wafer covered with a 300 nm SiO_2 layer. The experimental processes and set-up used in this work are shown in figure 1(a). Commercial sulfur and sodium molybdate were used as the precursors in a two temperature-zone furnace. The initial concentration of the sodium molybdate-based solution was controlled for the selective growth of the MoS_2; Group 1(G1), Group 2(G2), Group 3(G3), and Group 4 (G4) were done with precursor concentrations of 0.1 g/50 ml, 0.1 g/80 ml, 0.1 g/110 ml, and 0.1 g/150 ml, respectively.

The optical images of the large-area CVD-grown monolayer MoS_2 with different initial precursor concentrations are shown in figures 1(b)–(e). Different

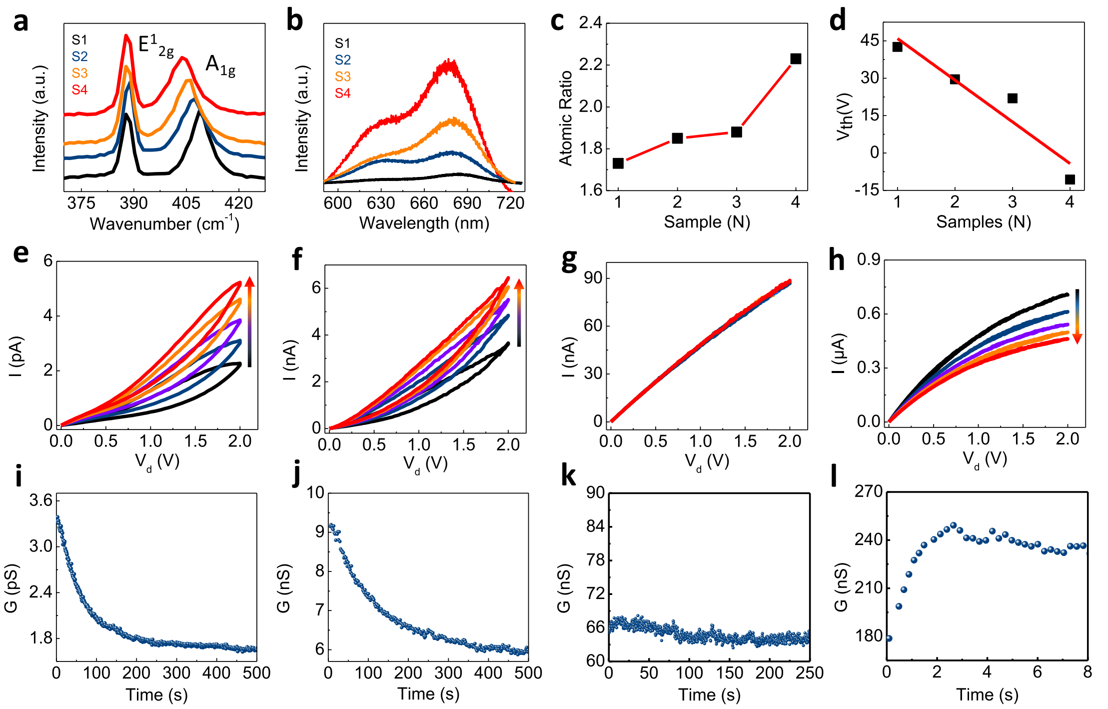

Figure 2. Electrical and optical characterizations of the four different groups (G1–G4) of the monolayer MoS_2. (a) and (b) The evolution of the Raman and PL spectra for sample of G1–G4, respectively. (c) The atomic ratio revealed by XPS spectrum for these four types of samples. (d) The corresponding threshold gate bias. (e)–(h) Successive I_d–V_d sweeps for G1–G4, respectively. The arrows represent the variation trend of current. (i)–(l) The evolution of the channel conductance measured by a small voltage of 0.5 V.

transfer curves, which indicates different carrier densities in the MoS_2, are shown in figure S2, highlighted by the tangential lines in the figures. The threshold gate bias, V_{th}, defined as an intersection between the tangential lines and the *x*-axis, changes over a wide range from 40 V to −10 V; based on the parallel capacitor model, the different V_{th} in figure S2 implies different carrier densities in the MoS_2 channel.

The origin of the diverse carrier doping density is attributed to the ratio of the Mo and S atoms in the MoS_2 grown by our CVD. Figures 2(a) and (b) show the Raman and Photoluminescence (PL) spectra of the four (G1–G4) samples. The E^1_{2g} mode is kept constant, and the A_{1g} mode demonstrates a clear red shift from G1 to G4 sample. The Raman peak separation between the E^1_{2g} and A_{1g} mode is ~16.12 cm^{-1} for G4 and increases gradually to ~20.87 cm^{-1} for G1 sample. In the PL spectra, the A exciton peak shifts from ~677 nm to ~685 nm, and the PL intensity (the absolute value for exciton A peak) varies by 16 times. The Raman and PL spectra imply a variation in the carrier concentration in the four samples (G1–G4) [29–32]. The x-ray photoelectron spectroscopy (XPS) of the four samples (G1–G4) is shown in figure S3, and the calculated atomic ratios of the Mo and S atoms shown in figure 2(c) are consistent with the carrier densities of the four samples, which is consistent to the different doping effect displayed in figure 2(d). It has been known that the S vacancy could generatre n-type doping or pin its Fermi level near the conductance band minimum [33]. Depending on the amount of S vacancies, different doping level in monolayer MoS_2 could occur. For example, the 9% S vacancy could make the carrier density of 7×10^{14} cm^{-2} and the geometry of the MoS_2 keep this triangular shape [33]. For our samples, we did not reach out such a doping level, and that is why the different groups of samples are almost triangular shape. Moreover, we note there are multilayer area in our samples (particular for G1 and G2), but when we characterizaed our samples, to avoid any sample thickness difference involved, including both of optical and electrical characterzation, we selected only monolayer regions to clearly exclude this possibility.

Continuous source-drain current and voltage (I_d–V_d) sweeps from 0 V to 2 V with the monolayer MoS_2 samples (marked as G1–G4 in figures 1(b)–(e)) without gate bias (or $V_g = 0$ V) are shown in figures 2(e)–(h). The colored arrows in figures 2(e)–(h) indicate a current increase (figures 2(e) and (f)) or a current decrease (figure 2(h)) as we repeat the I_d–V_d sweeps. We interpret the conductance change by the Joule-heating effect [26]. The first sweeps (black curves in figures 2(e)–(h)) already show a semiconducting behavior in figures 2(e) and (f), and a metallic behavior in figure 2(h); the resistive-heating effect on semiconductors and metals causes the different two-probe I_d–V_d characteristics [26, 34, 35].

To confirm the hypothesis of the resisitive-heating effect, we conducted low temperature transport measurements shown in figure S4; the monolayer MoS_2 devices do not show any conductance dynamics or

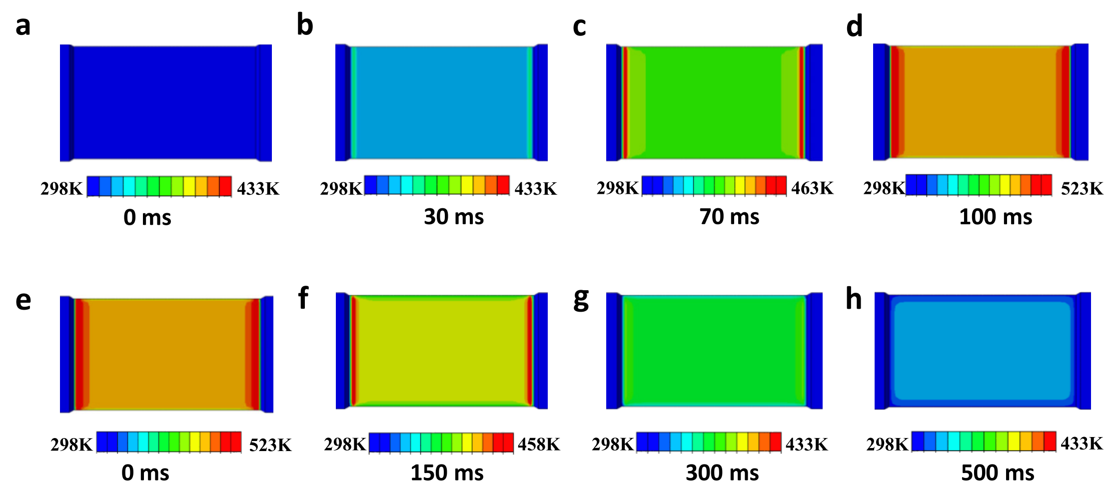

Figure 3. Simulation results of the temperature evolution induced by Joule-heating in the monolayer MoS_2 when a pulse voltage is applied. The pulse voltage with an amplitude of 5 V and a width of 100 ms was used as stimulus. (a)–(d) Heating-up: the Joule-heating-driven temperature evolution after stimulation by the pulse voltage in a two-terminal monolayer MoS_2 device. A higher temperature near the contact area is observed. (e) and (h) Cooling down: the natural cooling down of the channel materials after the stimulus of the pulse voltage. The temperature in the channel can be naturally cool down to room temperature. RT represents room temperature. The blue areas at the two ends of each figure represents the Au contacts.

short-term synaptic plasticity at a temperature of 80 K. Moreover, figure S5 shows the temperature-dependent conductance of the active MoS_2 channel in a temperature range of 280 to 440 K, and the conductance changes by about 3.5 times at $T = 440$ K compared with its conductance at $T = 280$ K, which is consistent with the conductance plasticity shown in figure 2(e). We also note that other mechanisms such as charge trap cannot explain the conductance increase (figures 2(e) and (f)) and the decrease (figure 2(h)) depending on the carrier density. Furthermore, for the role of doping and temperature in the electrical response in the transport channel, metal-insulator transition (MIT) should be considered [36]. In MoS_2, there is a critical doping concentration for MIT. Below this specific doping level, the conductance of MoS_2 increases with the temperature incresing, which is a typical behavior of s semiconductor. However, above this doping level (carrier concentration), it decreases with the temperature increasing, which indicates a metallic behavior from a degenerate semiconductor. Therefore, the conductance plasticity highly depends on the carrier concentrations in the MoS_2. We carried out the gate voltage dependent correaltions between conductance and temperature. It is clearly shown that when the gate voltage varies (different doping level), the conductance plasticity is different, which proves that the different amount of S vacancies in our different groups of samples could have different conductance plasticity potential, which could be used to mimic the different synaptic strengths.

As we understood the conductance dynamics by the resistive-heating effect, natural (air-based) cooling of the active channel, after stopping the voltage sweep up to 2 V, is expected. Indeed, the conductance is reset to its original value automatically shown in figures 2(i)–(l) with characteristic time constants, which could be interpreted as a consequence of the natural cooling of the channel. We note that applying a small V_d (e.g. 0.1 V) does not produce the Joule-heating effect, which enables us to study the conductance dynamics without altering the residual temperature of the channel by high voltages.

Together with the working mechanism, figures 2 (e)–(h) reveal that the carrier concentration in the active semiconducting channel is critical to emulate different strengths of synaptic plasticity or connectivity. In the case of a high carrier density of the active MoS_2 channel, for example, a metallic behavior appears; the conductance gradually decreases when the channel temperature increases by applying a high V_d of 2 V or repeating the I_d–V_d sweep up to $V_d = 2$ V (figure 2(h)). This is consistent with a previous report on the metal-insulator transition (MIT) in MoS_2 by its carrier concentration [26]. With the carrier concentration gradually increasing from figures 2(e)–(g), the conductance plasticity becomes weaker, and there is almost no conductance plasticity in figures 2(g) and (k); this means the carrier concentration in figures 2(g) and (k) is near the critically point of MIT [26, 34, 35]. With a further increased carrier concentration of the MoS_2, the monolayer MoS_2 totally shows a metallic behavior (figures 2(h) and (l)); as we repeat the I_d–V_d sweeps, the conductance decreases. In each I_d–V_d sweep, the conductance (the tangential slopes in figure S2(d)) also decreases at a higher V_d.

We conducted a simulation on the conductance dynamics based on resistive-heating in our two-terminal device geometry with the monolayer MoS_2 as shown in figure 3. The evolution of resistive-heating as a function of time could be simulated as described in figures 3(a)–(d). The pulse voltage and its time width were 5 V and 100 ms, respectively in the simulation. It is clearly observed that the residual temperature

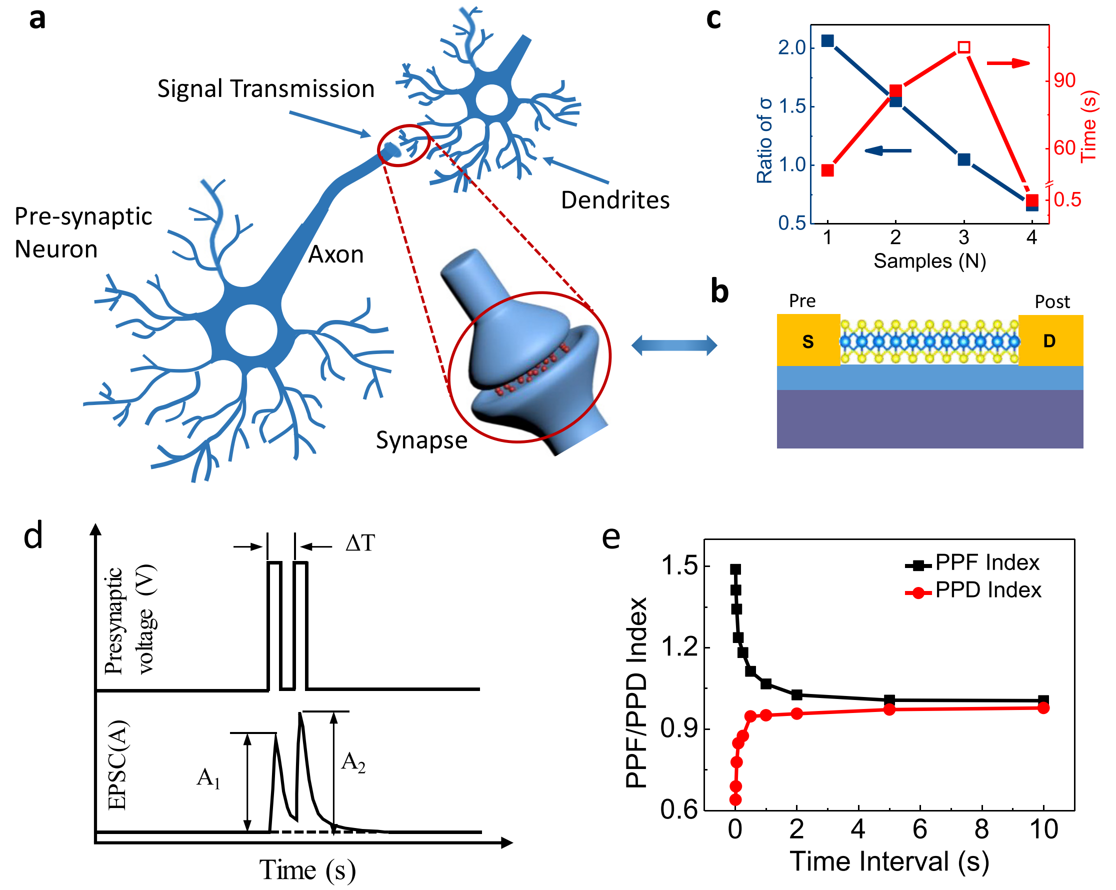

Figure 4. (a) Schematic diagram for the synaptic transmission between two adjacent neurons. (b) The two-dimensional device structure used for mimicking synaptic transmission in this work. (c) The conductance plasticity ratio and the tunable time constants described in figures 2(e)–(h). (d) A pair of presynaptic spikes with a specific time interval and the corresponding triggered EPSC. (e) PPF and PPD indexes after stimulated by two continuous pulses. The different time intervals of these two consecutive pulses ranges from 10 ms to 10 s, respectively.

increases in the channel, which is dominant near the metal electrodes; the contact resistance drives the resistive-heating in the series connection of the electric channel and contacts shown in figure S6. Therefore, the influence of channel length on the joule heating in channel could be negligible. The *I*–*V* curve of another device with small channel length (~50 nm) is shown in figure S7 and the condutance plasticity due to joule heating could be seen clearly. The temperature in the channel was calculated as $T = 473$ K shown in figure 3(d), which is consistent to the temperature range and conductance changes (3–5 times) described in figures 2 and S5. Natural cooling was also simulated shown in figures 3(e)–(h) with a characteristic time of 500 ms. Accordingly, the conductance facilitation and depression in figure 2 could be understood based on the simulation studies.

Using the resistive-heating energy given by the formula ($Q = I^2R$) and the heat capacity of the monolayer MoS_2 ($Q = Cm\Delta T = C\rho V\Delta T$) where C, ρ, and V are the specific heat, mass density, and the volume of the monolayer MoS_2, we calculated an expected temperature of $T = 803$ K. The experimentally estimated temperature (~473 K) is lower than the calculated temperature probably due to the heat dissipation through the SiO_2 substrate and the air convection.

From the discussion above, we realized diverse conductance plascitity of monolayer MoS_2 by selective growth technique, which could be used to mimic the synapse. As shown in figure 4(a), the synapse links two adjacent neurons; neurotransmitters are released from the presynaptic neuron into the postsynaptic neuron when the the action potential is achieved in the presynaptic neuron. The information transmission process is described by a device structure as shown in figure 4(b). The source electrode with a certain of voltage emulates the release of neurotransmitters from the presynaptic neuron, and the signal is collectd by the drain electrode (postsynaptic neuron) throught the MoS_2 channel, which can be considered as information transmision in figure 4(a).

In our samples, the conductance ratios between before and after a Joule heating, and the time constants of the plasticity (the time required for the decay of the maximum conductance to its half value) of samples of G1–G4 are summarized in figure 4(c). For sample of G1–G2, the conductance ratio is larger than ‘1’ due to their semiconducting nature; The sample of G3 shows almost a conductance ratio of ‘1’ as we discussed in figures 2(g) and (k). However, the sample of G4, having the highest carrier concentration among the four samples, exhibits a conductance ratio of less than ‘1’ in

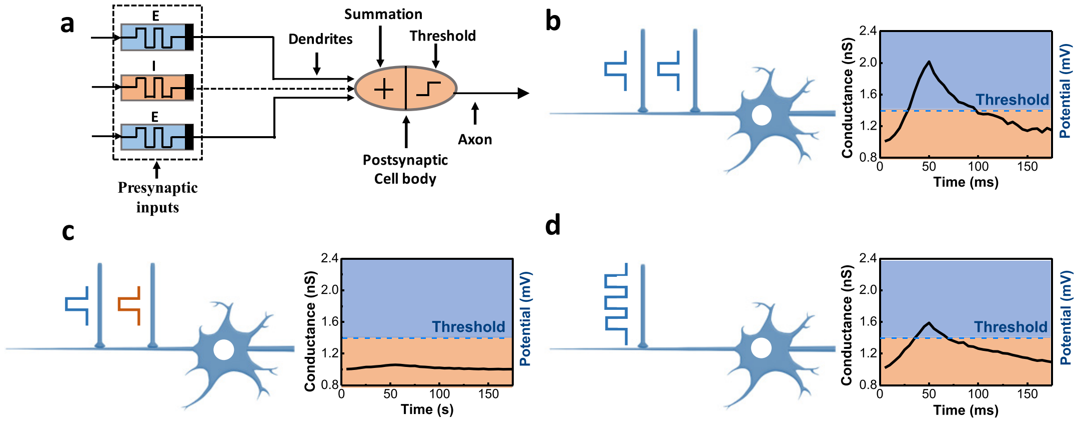

Figure 5. The synaptic spatiotemporal summation as an example of artificial neural networks with the monolayer MoS_2. (a) Schematic of the presynaptic input and dendrite connected to a postsynaptic cell body (neuron) with an axon. The dendrites receive inputs from the synaptic synapse network mimicked by our monolayer MoS_2-based devices. (b) Spatial summation of two excitatory synapses. (c) Spatial summation of one excitatory synapse and one inhibitory synapse. (d) Temporal summation based on one excitatory synapse. Their corresponding conductance plasticity with the different inputs are shown in '(b)–(d)'. The blue lines in (b)–(d) represent the threshold level of firing in the target neuron.

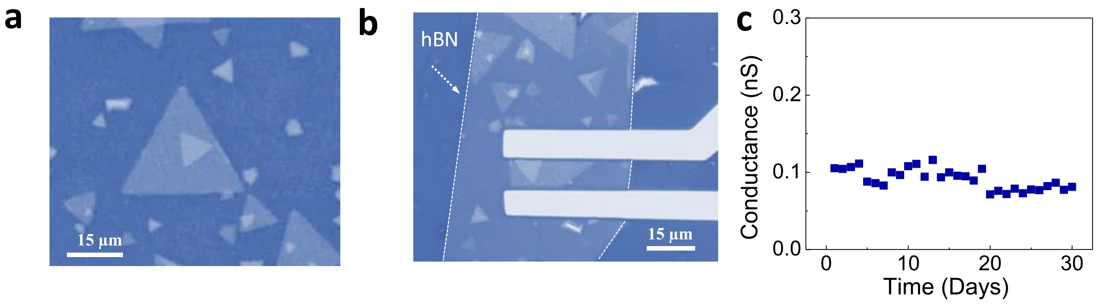

Figure 6. MoS_2 with artificially made partial bilayer regions. (a) Optical image of artificially constructed MoS_2 flakes with partial bilayer regions. (b) Optical image of a device after passivation by a few layers of h-BN. The dashed lines show the edges of h-BN. (c) Stability of the device after passivating with a few layers of h-BN. The conductance is stable over one month.

figure 4(c) reflecting a metallic behavior (figures 2(h) and (l)).

Concerning the characteristic times, increasing time constants are observed from samples of G1 to G3; these increases are due to the different cooling processes of the active channel with different carrier densities. In particular, because there is almost no conductance plasticity in the sample of G3, the time constant becomes infinite in figure 4(c), we used a hollowed pink square to represent the infinite time. The sample of G4 exhibits a short time constant due to its fast cooling of the metallic MoS_2 compared to that of the semiconducting MoS_2. Such conductance ratios higher and lower than 1 (blue rectangles in figure 4(c)) emulates the excitatory/inhibitory synapes, respectively.

This realizes two basic synaptic computation: paried pulse facilitation (PPF) and depression (PPD), defined as A_2/A_1, to evaluate the strength of synaptic plascitity, where A_1 and A_2 are the absolute amplitudes of excitatory/inhibitory postsynaptic current when excited by two continous presynaptic impulses, respectively, as shown in figures 4(d) and (e). The voltage amplitude and width used in this measurements are 25 V and 50 ms, respectively. Figure 4(e) shows that the strength of synaptic plasticity highly depends on the time interval of two impluses.

By using the two types of synaptic plasticity, we demonstrated synaptic spatiotemporal summation, a synaptic network for diverse cognitive behaviors, based on our monolayer MoS_2 having controllable synaptic plasticity. The synaptic computation includes synaptic potentiation (excitatory synapse, ES), depression (inhibitory synapse, IS) with diverse characteristic times. A schematic picture of an artificial target neuron with a synaptic network is shown in figure 5(a) where a combination of ES and IS determines the postsynaptic input for the target neuron [37, 38], which is called 'synaptic summation' [38, 39].

A synaptic circuit with two ESs, a spatial synaptic summation, is demonstrated in figure 5(b). An overlap of synaptic facilitation from the sum of two ESs, as a postsynaptic input for the target neuron, could be generated, and the postsynaptic input signal easily overcomes the threshold membrane potential of the target neuron. On the other hand, a spatial synaptic summation with combination of one ES and one IS produced a compensated signal from the synaptic facilitation (ES) and depression (IS); the postsynaptic input from the compensation cannot overcome the threshold membrane potential of the target neuron (figure 5(c)). We note that this is the first demonstration of circuit-based synaptic transmission engineering by single ES and IS monolayered two-terminal devices. Another temporal synaptic summation with several repeated stimuluses as inputted signal is demonstrated in figure 5(d) where the overall behaviors are similar to that demonstrated in figure 5(b). The optical images of the corresponding device are shown in figure S8. Moreover, to avoid the effect of ambient, we use the h-BN, which is the most stable 2D materials, to passivate the device, as shown in figures 6 and S1, the stable operation is over 30 d.

4. Conclusions

In summary, selective CVD growth of monolayer MoS_2 based on a simple precursor density control was developed for constructing efficient and integrated synaptic networks. Each MoS_2-based synaptic device in the synaptic networks has two-terminal geometry, allowing an easy integration and the emulation of ES and IS. The control of the doping level through the CVD process induces the electronic phase transition (MIT) in the MoS_2 that enables the engineering of synaptic plasticity for ES and IS synaptic devices. We demonstrated a neurophysiologic behavior for basic spatiotemporal synaptic summation circuits with the MoS_2-based devices. The fundamental origin of the synaptic plasticity with the MoS_2 was found to be energy-efficient resistive-heating of the two-dimensional material, particularly, near the junctions with the electrodes. Our work paves the way to mimic the complex cognitive processes in the brain.

Acknowledgments

This work is supported by the Samsung Research Funding & Incubation Center of Samsung Electronics under project no. SRFC-MA1701-01. L F Sun acknowledges support from the Korea Research Fellowship Program through the National Research Foundation of Korea (NRF) funded by the Ministry of Science and ICT under grant no. NRF-2017H1D3A1A01013759.

Conficts of interest

There are no conficts to declare.

Electric supplementary information

Electric supplementary information (ESI) available.

ORCID iDs

Qi Ge https://orcid.org/0000-0002-8666-8532

Heejun Yang https://orcid.org/0000-0003-0502-0054

References

[1] Abbott L F and Regehr W G 2004 *Nature* **431** 796
[2] Indiveri G and Liu S 2015 *Proc. IEEE* **103** 1379
[3] Merolla P A *et al* 2014 *Science* **345** 668
[4] Furber S B, Galluppi F, Temple S and Plana L A 2014 *Proc. IEEE* **102** 652
[5] Jo S H, Chang T, Ebong I, Bhadviya B B, Mazumder P and Lu W 2010 *Nano Lett.* **10** 1297
[6] Rajendran B, Liu Y, Seo J, Gopalakrishnan K, Chang L, Friedman D J and Ritter M B 2013 *IEEE Trans. Electron Devices* **60** 246
[7] Blitz D M, Foster K A and Regehr W G 2004 *Nat. Rev. Neurosci.* **5** 630
[8] Wu S, Wong K Y M and Tsodyks M 2013 *Frontiers Comput. Neurosci.* **7** 188
[9] Jackman S L and Regehr W G 2017 *Neuron* **94** 447
[10] Deco G, Rolls E T and Romo R 2010 *Proc. Natl Acad. Sci.* **107** 7545
[11] Deco G, Rolls E T, Albantakis L and Romo R 2013 *Prog. Neurobiol.* **103** 194
[12] Anwar H, Li X, Bucher D and Nadim F 2017 *Curr. Opin. Neurobiol.* **43** 71
[13] Yang Y, Cui Y, Sang K, Dong Y, Ni Z, Ma S and Hu H 2018 *Nature* **554** 317
[14] Boegerhausen M, Suter P and Liu S-C 2003 *Neural Comput.* **15** 331
[15] Saïghi S *et al* 2015 *Frontiers Neurosci.* **9** 227
[16] Burr G W *et al* 2017 *Adv. Phys.* X **2** 89
[17] Kuzum D, Jeyasingh R G D, Lee B and Wong H S P 2012 *Nano Lett.* **12** 2179
[18] Ohno T, Hasegawa T, Tsuruoka T, Terabe K, Gimzewski J K and Aono M 2011 *Nat. Mater.* **10** 591
[19] van de Burgt Y, Lubberman E, Fuller E J, Keene S T, Faria G C, Agarwal S, Marinella M J, Alec Talin A and Salleo A 2017 *Nat. Mater.* **16** 414
[20] Sangwan V K, Jariwala D, Kim I S, Chen K-S, Marks T J, Lauhon L J and Hersam M C 2015 *Nat. Nano* **10** 403
[21] Kumar S, Strachan J P and Williams R S 2017 *Nature* **548** 318
[22] Yoshida M, Suzuki R, Zhang Y, Nakano M and Iwasa Y 2015 *Sci. Adv.* **1** e1500606
[23] Tian H *et al* 2017 *ACS Nano* **11** 7156
[24] Jie J, Junjie G, Xiang W, Yi Y, Haipeng X, Dongmei N, Junliang Y, Jun H, Yongli G and Qing W 2017 *Small* **13** 1700933
[25] Sangwan V K, Lee H-S, Bergeron H, Balla I, Beck M E, Chen K-S and Hersam M C 2018 *Nature* **554** 500
[26] Sun L, Zhang Y, Hwang G, Jiang J, Kim D, Eshete Y A, Zhao R and Yang H 2018 *Nano Lett.* **18** 3229–34
[27] Zucker R S and Regehr W G 2002 *Annu. Rev. Physiol.* **64** 355
[28] Fioravante D and Regehr W G 2011 *Curr. Opin. Neurobiol.* **21** 269
[29] Amani M *et al* 2015 *Science* **350** 1065
[30] Sun L, Zhang X, Liu F, Shen Y, Fan X, Zheng S, Thong J T L, Liu Z, Yang S A and Yang H Y 2017 *Sci. Rep.* **7** 16714
[31] Nan H *et al* 2014 *ACS Nano* **8** 5738
[32] Chakraborty B, Bera A, Muthu D V S, Bhowmick S, Waghmare U V and Sood A K 2012 *Phys. Rev.* B **85** 161403
[33] Voiry D *et al* 2016 *Nat. Mater.* **15** 1003
[34] Grosse K L, Bae M-H, Lian F, Pop E and King W P 2011 *Nat. Nanotechnol.* **6** 287
[35] Islam S, Li Z, Dorgan V E, Bae M H and Pop E 2013 *IEEE Electron Device Lett.* **34** 166
[36] Yang H, Kim S W, Chhowalla M and Lee Y H 2017 *Nat. Phys.* **13** 931
[37] Longordo F, To M-S, Ikeda K and Stuart G J 2013 *Nat. Neurosci.* **16** 714
[38] Magee J C 2000 *Nat. Rev. Neurosci.* **1** 181
[39] Poirazi P, Brannon T and Mel B W 2003 *Neuron* **37** 977